The Astrophysical Journal Supplement Series, 269:52 (10pp), 2023 December https://doi.org/10.3847/1538-4365/ad0633
© 2023. The Author(s). Published by the American Astronomical Society.
OPEN ACCESS

Spacecraft Floating Potential Measurements for the Wind Spacecraft

Lynn B. Wilson III[1], Chadi S. Salem[2], and John W. Bonnell[2]
[1] NASA Goddard Space Flight Center, Heliophysics Science Division, Greenbelt, MD 20771, USA; lynn.b.wilsoniii@gmail.com
[2] Space Sciences Laboratory, University of California, Berkeley, CA 94720-7450, USA
Received 2023 September 21; revised 2023 October 20; accepted 2023 October 20; published 2023 November 30

Abstract

Analysis of 8,804,545 electron velocity distribution functions, observed by the Wind spacecraft near 1 au between 2005 January 1 and 2022 January 1, was performed to determine the spacecraft floating potential, ϕ_{sc}. Wind was designed to be electrostatically clean, which helps keep the magnitude of ϕ_{sc} small (i.e., ∼5–9 eV for nearly all intervals) and the potential distribution more uniform. We observed spectral enhancements of ϕ_{sc} at frequencies corresponding to the inverse synodic Carrington rotation period with at least three harmonics. The two-dimensional histogram of ϕ_{sc} versus time also shows at least two strong peaks, with a potential third, much weaker peak. These peaks vary in time, with the intensity correlated with solar maximum. Thus, the spectral peaks and histogram peaks are likely due to macroscopic phenomena like coronal mass ejections (solar cycle dependence) and stream interaction regions (Carrington rotation dependence). The values of ϕ_{sc} are summarized herein and the resulting data set is discussed.

Unified Astronomy Thesaurus concepts: Solar wind (1534); Deep space probes (366); Heliosphere (711); The Sun (1693); Solar activity (1475)

1. Background and Motivation

The solar wind is a nonequlibrium, kinetic, ionized gas comprised of electrons and multiple ion species (with multiple charge states) from hydrogen up through iron (e.g., Bame et al. 1968; Bochsler et al. 1985; Gloeckler et al. 1998; Lepri et al. 2013). The solar wind is not in equilibrium because it is weakly collisional (e.g., Salem et al. 2003; Maruca et al. 2013), allowing for the consistent presence of finite heat fluxes, and the temperatures of species s' and s are not equal, i.e., $(T_{s'}/T_s)_{tot} \neq 1$, for $s' \neq s$ (see Appendix A for parameter definitions; e.g., Wilson et al. 2018, 2019a, 2019b).

Spacecraft propagating through space experience a net charging, called the spacecraft potential or ϕ_{sc} (e.g., Grard 1973; Besse & Rubin 1980; Garrett 1981; Whipple 1981; Grard et al. 1983; Scime et al. 1994; Pedersen 1995; Scudder et al. 2000; Salem et al. 2001; Génot & Schwartz 2004; Geach et al. 2005; Pulupa et al. 2014; Lavraud & Larson 2016; Lai et al. 2017). On average, when the spacecraft is in sunlight there is a net-zero current balance between the ambient plasma and the spacecraft. The current sources are thermal currents from ambient plasma species, $j_{th,s}$, bulk flow velocity currents if in regions like the solar wind, $j_{o,s}$, photoelectron currents due to the photoelectric effect, j_{ph}, and currents from emission of secondary particles from impact ionization $j_{2nd,s}$. The magnitude of ϕ_{sc} depends upon the electromagnetic cleanliness of the spacecraft, the space environment, and whether the spacecraft is in sunlight or the shadow of some object. Generally, however, the better the electromagnetic cleanliness the smaller in magnitude ϕ_{sc} will be, on average. An accurate measure of ϕ_{sc} is critical for properly calibrating thermal electron detectors and calculating accurate electron velocity moments (e.g., Scime et al. 1994; Salem et al. 2001; Génot & Schwartz 2004; Geach et al. 2005; Pulupa et al. 2014; Lavraud & Larson 2016).

Original content from this work may be used under the terms of the Creative Commons Attribution 4.0 licence. Any further distribution of this work must maintain attribution to the author(s) and the title of the work, journal citation and DOI.

Modern spacecraft equipped with electric field probes can directly measure ϕ_{sc} versus time, e.g., the Magnetospheric Multiscale mission (e.g., Ergun et al. 2016; Lindqvist et al. 2016). This requires a constant measurement of the quasi-static, DC-coupled electric potential versus time. Many earlier spacecraft were much more restricted in onboard memory, telemetry rates, and receiver electronics. Thus, it is often required that researchers infer the spacecraft potential by relying on discrepancies between two measurements of the same quantity[3] (see, e.g., Salem et al. 2001, 2023) or by directly measuring the separation between ambient and photoelectrons with something like a thermal electron detector (e.g., Phillips et al. 1993). The former technique requires both instruments be very well calibrated, while the latter technique requires the instrument minimum energy, E_{min}, be smaller than ϕ_{sc} for all $\phi_{sc} > 0$ eV.

For most spacecraft operating in the solar wind, there are few (if any) energy bins that satisfy $E \leqslant \phi_{sc}$, so the proper shape or form of the velocity distribution function (VDF) for the photoelectrons is not well known (e.g., Phillips et al. 1993). The simplest approach is to model them as a single, isotropic Maxwell–Boltzmann distribution (e.g., Grard 1973; Halekas et al. 2020; Wilson et al. 2022). There is some evidence that the photoelectron distribution in the solar wind is not a single Maxwellian but may be at least two populations (C. S. Salem et al. 2023, in preparation), consistent with magnetospheric observations (e.g., Pedersen 1995). However, it is beyond the scope of the current study to determine the shape of this photoelectron VDF, though it is a topic of active investigation.

This paper is structured as follows. Section 2 introduces the data sets and methodology; Section 3 presents some preliminary long-term solar wind statistics; and Section 4 discusses the results and interpretations, with recommendations for future measurement/instrumentation requirements. Appendices are also included

[3] Often it is the difference between the total electron density derived from the quasi-thermal noise upper hybrid line and the measured density from a particle instrument.

to provide additional details of the parameter definitions (Appendix A), some additional one-variable statistics (Appendix B), and a detailed description of the public data set generated from the analysis in this study (Appendix C).

2. Data Sets and Methodology

2.1. Data Sets

Nearly all data presented herein were measured by the Wind spacecraft (Wilson et al. 2021) near 1 au in the solar wind, specifically the thermal electron detector EESA Low, part of the 3DP instrument suite (Lin et al. 1995). The data are taken from both burst and survey modes, which have cadences of ~3 s and ~24–78 s, respectively.[4] All EESA Low distributions have spin-period durations or total integration times (i.e., ~3 s for the entire mission). All VDFs have 15 energy bins and 88 solid angle look directions, with typical resolutions of $\Delta E/E$ ~20% and $\Delta\phi$ ~5°–22.5° depending on the poloidal anode (i.e., the ecliptic plane bins have higher angular resolution than the zenith). All in situ measurements presented herein are shown in the spacecraft frame of reference.

We also present observations of solar emission lines from the Thermosphere Ionosphere Mesosphere Energetics Dynamics (TIMED) spacecraft, specifically the Solar EUV Experiment (SEE; Woods et al. 2005). The data are used as a proxy for solar cycle and variations in ionizing photon and photoelectron flux versus time.

We examined all electron energy distribution functions (EDFs) between 2005 January 1 and 2022 January 1, corresponding to a total of 8,804,545 EDFs. We chose this time range because the start is well after Wind moved to the first Sun–Earth Lagrange point permanently and the detector E_{min} was below ~6 eV. The lower bound on E_{min} ranged from ~3.2 to 5.2 eV for all EDFs examined. It is critical that $E_{min} < \phi_{sc}$, otherwise we can only define an upper-bound estimate for ϕ_{sc} from the thermal electron measurements.

2.2. Photoelectron Identification

All EDFs were plotted to a computer screen and viewed, "by eye," in rapid succession to determine some overarching properties of the electrons.[5] Several important features were observed from this effort. The first is that $\phi_{sc} < 30$ eV for nearly every EDF of the 8,804,545 EDFs examined herein. Thus, we imposed an a priori maximum energy, E_{max}, for any ϕ_{sc} solution of 30 eV.[6] Second, we observed that the EDFs had four characteristic shapes/profiles (discussed in more detail below) that allowed us to simplify our approach.

To provide the reader with some context, Figure 1 shows an example EDF with example model predictions for the photoelectrons. The electron data are shown as the thin, multicolored lines, while the photoelectron model and ϕ_{sc} solution are shown with thick, color-coded lines. The data are shown in units of phase space density for ease of modeling since these are the natural units of a Maxwell–Boltzmann distribution. The details of the model are discussed in Wilson et al. (2022). The model parameters are shown in the figure legend in the upper-right-hand corner of the plot (see Appendix A for symbol definitions). The purpose of Figure 1 is to illustrate which parts of the EDF are photoelectrons versus ambient solar wind electrons.

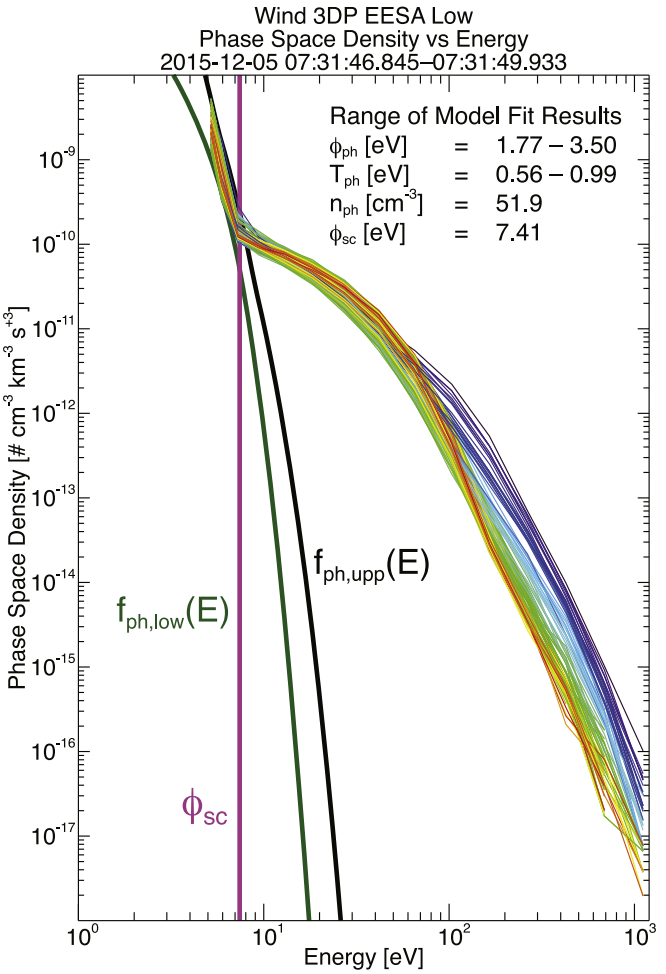


Figure 1. Example electron energy distribution function (EDF) from the Wind 3DP instrument. The multicolored thin lines show the phase space density (# cm^{-3} km^{-3} s^{+3}) of each of the 88 solid angle bins vs. energy, E (eV). The photoelectrons are seen to the left of the vertical magenta line marking the spacecraft floating potential, ϕ_{sc}. The thick green and black lines show simplified model EDFs for the photoelectrons (following the method in Wilson et al. 2022) with parameter ranges shown in the legend of the plot.

One may ask how we know the data falling between the thick green and black lines are photoelectrons and not some cold, ambient solar wind population. We can measure the total electron density, n_e, from the upper hybrid line (e.g., Meyer-Vernet & Perche 1989) observed by the Wind WAVES instrument (Bougeret et al. 1995). We can invert the frequency of this line, knowing the quasi-static magnetic field, to calculate the electron plasma frequency and thus the electron density. Doing this gives us n_e ~7.95 cm^{-3}. For comparison, a typical value for the photoelectron number density, n_{ph}, is >200 cm^{-3} and the mean kinetic energy of the photoelectrons, or their temperature, T_{ph}, is ~1 eV (e.g., Grard 1973; Grard et al. 1983).

To further illustrate why the electrons between the thick lines are not part of the ambient solar wind, we can numerically integrate the EDF following the usual approach of adjusting the distribution by ϕ_{sc} then calculating the velocity moments (see,

[4] All products discussed herein start from the Wind 3DP level zero files found at http://sprg.ssl.berkeley.edu/wind3dp/data/wi/3dp/lz/.

[5] The plots were viewed more like a high-frame-rate movie than a series of individual images to make the effort feasible.

[6] Previous solar wind estimates/measurements of ϕ_{sc} in the solar wind have typically fallen below ~10–15 eV (e.g., Pedersen 1995; Salem et al. 2001; Geach et al. 2005).

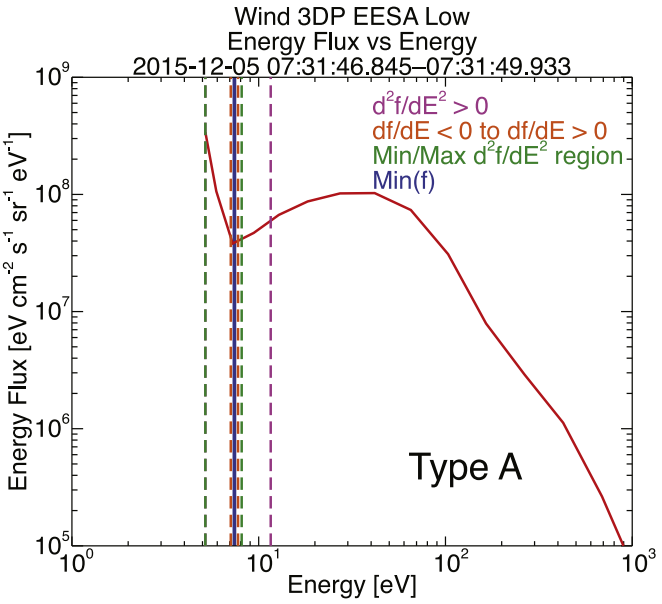


Figure 2. Illustrative example of an electron energy distribution function (EDF) showing the photoelectrons and the ambient electrons in the solar wind near 1 au. The red solid line shows the median of the energy flux, $f_e(E)$ (eV^{+1} cm^{-2} s^{-1} sr^{-1} eV^{-1}), at each energy over all 88 solid angle bins vs. energy, E (eV), on a log–log scale. The vertical lines indicate values or ranges of values for the estimated ϕ_{sc} of this EDF (see labels). The magenta lines (Method 1, see text for definition) show the region bounding the region of positive curvature (note left-hand bound covered by green dashed line). The orange lines show the region bounding the transition from negative to positive slope (Method 2). The green lines show the region bounding the minimum-to-maximum curvature transition (Method 3). Finally, the blue line shows the point of minimum in $f_e(E)$ (Method 4).

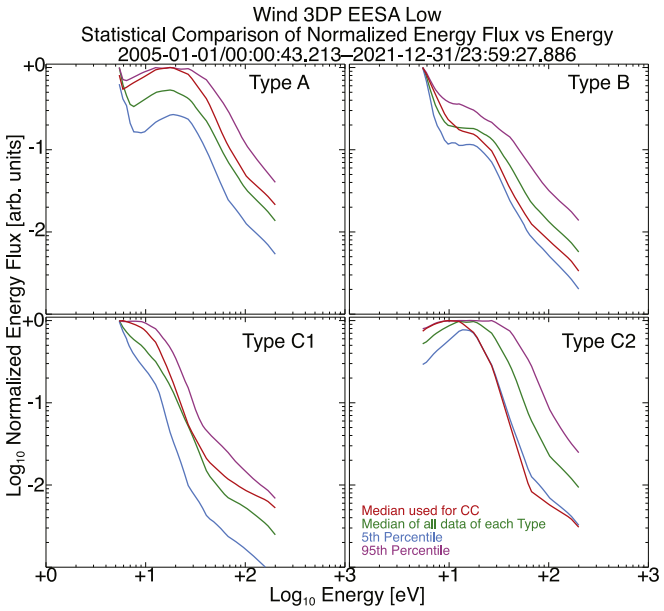


Figure 3. Characteristic EDFs representing the four shapes observed herein, shown as the red solid lines. All $f_e(E)$ were normalized to the peak magnitude prior to calculation for this figure. Type A is the ideal case, illustrated in Figure 2. Type B is the next best shape but often shows a shoulder or saddle point rather than a local minimum, increasing the uncertainty of the ϕ_{sc} estimates. Type C1 has $\phi_{sc} < E_{min}$ and the lowest-energy bin has $\frac{df}{dE} \sim 0$. Type C2 also has $\phi_{sc} < E_{min}$ but the lowest-energy bin has $\frac{df}{dE} > 0$. Both Types C1 and C2 are not considered useful shapes as we can only constrain the upper bound on ϕ_{sc}. The green line in each panel represents the median of all EDFs for each type. The blue (magenta) line in each panel represents the corresponding 5th (95th) percentile of all EDFs of each type.

e.g., Wilson et al. 2019b, 2022). We find the integrated velocity moments are $n_{e,int} \sim 7.01$ cm^{-3} and $T_{e,int} \sim 22.5$ eV. If we do not remove the photoelectrons and do not adjust the energies prior to integration, we find $n_{e,bad} \sim 39.2$ cm^{-3} and $T_{e,bad} \sim 7.34$ eV. Since the upper hybrid line density is ~ 7.95 cm^{-3}, it is clear that the electrons below ~ 7.41 eV are photoelectrons.

Figure 2 shows an example EDF to illustrate how we identify the region in energy filled by photoelectrons versus those with ambient electrons. The data in Figure 2 (solid red line) show the median at each energy of all the thin, multicolored lines (i.e., the 88 solid angle bins) from Figure 1 but in units of energy flux.[7] For brevity, we will call this $f_{med}(E)$. There are also multiple vertical lines in Figure 2, which will be explained below. Figure 2 is an ideal case where there is a clear discontinuity in the data, below which one sees a sharply increasing $f_e(E)$ with decreasing E. As explained in the discussion above and referenced citations, this "kink" in the EDF roughly marks the point corresponding to ϕ_{sc}.

2.3. Floating Potential Calculation

The EESA Low detector returns measurements for 88 solid angle look directions and 15 energy bins. To simplify and reduce computation requirements, we construct a pitch-angle distribution (PAD) for each EDF, where we average the solid angle look directions within ±22.5° of the parallel, perpendicular, and antiparallel directions (with respect to the quasi-static magnetic field vector, $\boldsymbol{B}_o$). This reduces the number of computations for each EDF by a factor of ~30. Note that when we examine an arbitrary EDF and view all 88 solid angles, the profiles/shapes are nearly always the same. That is, if one solid angle direction looks like the EDF in Figure 2, the other 87 will as well.

To keep the approach simple and focus on finding accurate but quick solutions for ϕ_{sc}, we use four methods to determine ϕ_{sc}, which is a rough boundary between photoelectron and ambient electrons. Note that each of the four ϕ_{sc} methods illustrated in Figure 2 will have at least three values. The four methods are as follows:

Method 1: find the range of energies where $\frac{d^2f}{dE^2} > 0$, or the positive curvature region (dashed magenta lines in Figure 2).

Method 2: find the range of energies where $\frac{df}{dE}$ transitions from negative to positive, i.e., find the local minimum of $f_e(E)$ (dashed orange lines in Figure 2).

Method 3: find the range of energies bounding the minimum and maximum values of $\frac{d^2f}{dE^2}$, i.e., the region of minimum and maximum curvature (dashed green lines in Figure 2).

Method 4: find the local minimum in $f_e(E)$ between E_{min} and E_{max} (solid blue line in Figure 2).

2.4. Assigning Type Labels

Figure 3 shows the EDF profiles of the four characteristic shapes we defined in this study (all lines have been normalized by their respective peak values). During the examination of the

[7] Energy flux was used when calculating ϕ_{sc} as the changes in $f_e(E)$ tend to be more pronounced than in units of phase space density.

EDFs, we observed two useful shapes that satisfy $E_{\min} < \phi_{sc}$ (i.e., Types A and B in Figure 3) and two not so useful shapes/profiles that satisfy $E_{\min} > \phi_{sc}$ (i.e., Types C1 and C2 in Figure 3). We chose, at random, one example EDF for each of the four characteristic shapes. We then calculated $f_{\text{med}}(E)$ (i.e., the same as done for Figure 2) to construct an example type, shown as the red lines in each panel of Figure 3. We then compared these example types to all 8,804,545 EDFs to assign the type labels accordingly (method for assignment discussed below). After the EDFs were assigned a type label, we needed to further validate that the assignments are correct. We calculated one-variable statistics of $f_{\text{med}}(E)$ at each energy for all EDFs in each type category.[8] For instance, for all EDFs labeled Type A, there will be N values of $f_{\text{med}}(E_j)$ at energy E_j. We can calculate the one-variable statistics of $f_{\text{med}}(E_j)$ to get things like the mean ($\bar{X}$), median ($\tilde{X}$), 5th percentile ($X_{5\%}$), 95th percentile ($X_{95\%}$), etc. (see Appendix A for symbol definitions). Then for, say, $X_{5\%}$ we can construct a line of 15 points (one for each energy) for this specific one-variable statistic value. We can do this for any of the one-variable statistic values. We chose the values of $X_{5\%}$, $\tilde{X}$, and $X_{95\%}$, which are shown as the blue, green, and magenta lines, respectively, in Figure 3. As one can see, the profile of the blue, green, and magenta lines for each EDF type follows that of the characteristic example used to assign the type label. Thus, the assignments are validated as being statistically correct.

We needed a quick method for identifying all the EDFs with an associated type label. This is necessary to determine which of the 8,804,545 values of ϕ_{sc} we can trust. The quickest approach is to calculate the cross-correlation coefficient (CC) between each characteristic example $f_{\text{med}}(E)$ (shown as red lines in Figure 3) and the $f_{\text{med}}(E)$ for all 8,804,545 EDFs. We do this in the following steps:

1. Normalize all 8,804,545 $f_{\text{med}}(E)$ by their respective peak values to avoid vertical offsets when comparing to each characteristic example $f_{\text{med}}(E)$ (also normalized by peak value).
2. Calculate 8,804,545 CCs for each characteristic example $f_{\text{med}}(E)$ allowing for seven energy offsets (i.e., allows each EDF to shift left and right in energy), generating a [N,7]-element array of CCs for each characteristic example $f_{\text{med}}(E)$.
3. Find the maximum CC by energy offset then by characteristic example $f_{\text{med}}(E)$ to determine the associated shape/type for each EDF.
4. Then ensure that the slope of the first few energy bins for Types A, B, and C2 match that expected from the characteristic example $f_{\text{med}}(E)$ (i.e., Types A and B must have a negative slope, Type C2 must have a positive slope).[9]

We did not bother with further constraints or complications because, as we will discuss below, there are many fewer Type C1 and Type C2 EDFs than Type A or Type B. The one-variable statistics of all EDFs for each type, shown as the blue, green, and magenta lines in Figure 3, indicate that our type label assignments are statistically correct.

[8] One can think of this as similar to a superposed epoch analysis but performed on EDFs. It allows us to statistically examine the EDFs from the resulting labeling scheme without checking each EDF "by eye" to ensure they exhibit the proper shape.

[9] Note that this slope requirement supersedes the CC magnitude ranking.

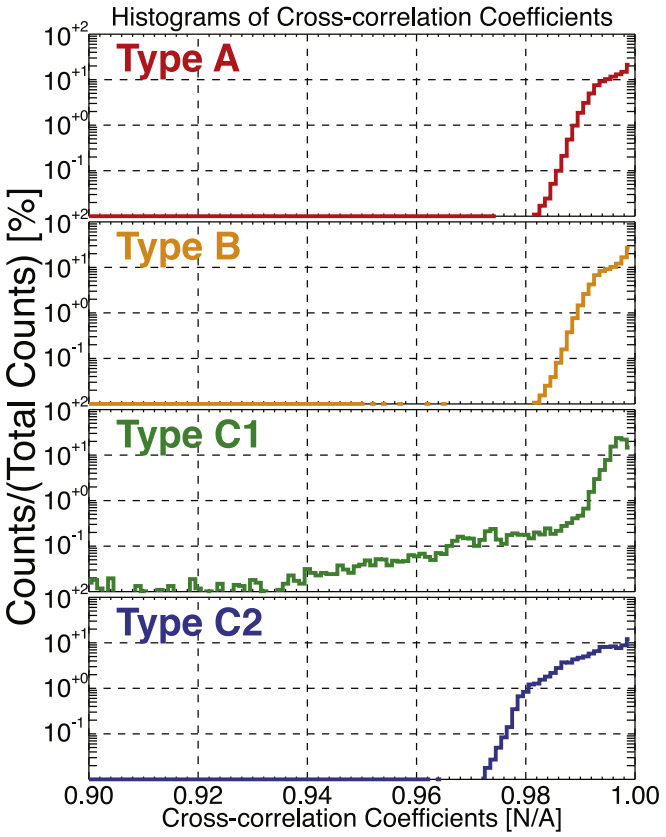


Figure 4. Histograms of the CC values for each type are shown as percentages of the total number of counts for each type.

The one-variable statistics of all CC values for each type are shown below in the form of $X_{5\%}$ to $X_{95\%}$ ($\bar{X}$)[$\tilde{X}$] (see Appendix A for symbol definitions):

Type A: 0.9915–0.9998(0.9965)[0.9969].
Type B: 0.9918–0.9998(0.9968)[0.9975].
Type C1: 0.9864–0.9996(0.9957)[0.9974].
Type C2: 0.9832–0.9997(0.9933)[0.9944].
Types C1 and C2: 0.9833–0.9997(0.9938)[0.9955].

Figure 4 shows the one-dimensional histograms of the CCs for each type, illustrating they have distinct distributions. For both Types A and B, the distribution is a narrow peak with ~95% of all CCs above ~0.991 and very weak (if any) tails to lower CC magnitudes. Both Types C1 and C2 had much broader peaks and stronger tails extending to lower CC magnitudes (especially C1). This further validates the identification scheme discussed above.

Thus, our labeling scheme identified, from all 8,804,545 EDFs, that there are as follows:

Type A: 4,014,873 (45.60%) EDFs.
Type B: 4,213,734 (47.86%) EDFs.
Type C1: 127,514 (1.45%) EDFs.
Type C2: 448,424 (5.09%) EDFs.
Types C1 and C2: 575,938 (6.54%) EDFs.

Given the small number of Type C1 and C2 EDFs, we did not further enhance the differentiation algorithms. The statistical shapes shown in Figure 3 illustrate that our algorithm works and that we have properly classified the EDFs. Therefore, we found no need to refine further.

Table 1
All EDF Types

ϕ_{sc} (eV)	X_{min} [a]	$X_{5\%}$ [b]	$\bar{X}$ [c]	$\tilde{X}$ [d]	$X_{95\%}$ [e]	X_{max} [f]
All 8,804,545 EDFs, Lower Bound						
Method 1	1.00	5.18	5.05	5.18	5.18	17.3
Method 2	1.00	5.42	7.98	7.09	12.1	27.1
Method 3	1.00	5.18	5.24	5.18	5.93	16.6
Method 4	4.91	5.93	8.03	7.41	12.7	29.7
All 8,804,545 EDFs, Upper Bound						
Method 1	4.91	16.6	28.5	29.7	29.7	29.7
Method 2	4.91	5.93	8.88	7.75	13.3	29.7
Method 3	4.91	5.93	12.7	12.7	18.1	29.7
Method 4	4.91	5.93	8.92	7.41	18.1	29.7

Notes. For symbol definitions, see Appendix A.
[a] Minimum.
[b] 5th percentile.
[c] Mean.
[d] Median.
[e] 95th percentile.
[f] Maximum.

We define a discrete quality flag for each set of ϕ_{sc} as follows:

QF = 4 All EDFs of Type A.
QF = 2 All EDFs of Type B.
QF = 0 All EDFs of Types C1 or C2.

Again, this is to simplify the process and use of the data set, to help the user determine whether to use or not use any given ϕ_{sc} solution. We did not feel it was useful to delineate the quality flags further as all Type Cs are one-sided constrained and all Type As are good. Type B solutions are reliable and most are good, though a few had weaker saddle points than others, and thus we used a less confident QF than for Type A.

3. Solar Wind Statistics

In this section, we present some preliminary statistical analysis of our ϕ_{sc} estimates.

Table 1 shows the one-variable statistics of ϕ_{sc} for all 8,804,545 EDFs, i.e., not distinguishing by EDF type.[10] Recall that Methods 1–3 provide ranges, which give the the upper and lower bounds in Table 1. As discussed before, Methods 1–3 provide a range of values, while Method 4 is a single value. However, all of these have three solutions for each of the three pitch-angle ranges discussed in Section 2. To provide a range of values for Method 4, we take the minimum and maximum values of E from the three pitch angles. We can then calculate one-variable statistics for each of the methods for all EDFs or by type and provide a range of values for each one-variable statistic variable (e.g., this is in reference to the values shown in Table 1). Note that the $\tilde{X}$ values for Method 2 and Method 3 nicely bound the values for Method 4. Method 1 has a much broader range of values, but this is not surprising as Method 1 can be ill-constrained except for EDF Types A and C2. The main takeaway here is that the spacecraft potential for the Wind spacecraft near 1 au in the solar wind typically satisfies $5\,\mathrm{eV} \lesssim \phi_{sc} \lesssim 13\,\mathrm{eV}$, consistent with previous studies (e.g., Pedersen 1995; Salem et al. 2001; Geach et al. 2005).

Figure 5 shows the two-dimensional histograms of the ϕ_{sc} estimates for Methods 1–4 (shown in order). The histogram bin sizes are 4 weeks for the horizontal (time) axis and ∼2 eV (i.e., 16 uniformly sized bins between 0 eV and 30 eV) for the vertical axis. White bins indicate no data whereas colors are quantified in the logarithmic scale to the right. Note that blue and purple are only a few tens of counts to single digits whereas the yellow-to-red portion are in the thousands. Thus, the latter are statistically significant while the former have low signal-to-noise ratios.

Recall that Methods 1–3 result in a range of values, i.e., two per EDF. Therefore, to construct these histograms for Methods 1–3, we calculate the median over the three PAD directions first, then take the average of the range of values. For Method 4, we take the median from the three pitch angles and then construct the histogram. The bottom two panels show solar irradiance measurements over the wavelength range of 0.1–7.0 nm (Diode 1) and ∼58.4 nm (He I) observed by the TIMED SEE experiment.

Note that Method 1 has, by construction, the largest range of values and often is bounded by the instrument E_{min} and our assumed E_{max} values. For EDFs of Types C1 and C2, the lower bound for Methods 1–3 is often 1 eV.[11] The midpoint over the range of energies allowed is 15 eV. This is why there is a high density of counts near 15 eV for Method 1. Since these are constructed using 4 week bins, each column can have multiple values, but this does not imply structure in the photoelectron part of any individual EDF. That is, finite counts in multiple rows of the histograms indicate that during any given 4 week interval (i.e., one column), ϕ_{sc} varied a lot.

For EDFs of Type A, Methods 2–4 are consistent with Method 2 and Method 3 bounding Method 4. This is largely why these three methods show a strong peak below ∼10 eV for all times. For EDFs of Type B, Method 2 and Method 4 are in the best agreement while Method 3 has difficulty limiting the bounds of ϕ_{sc}. Note that the repeated value of ∼4.91 eV in Table 1 corresponds to ∼95% of most E_{min} detector values. This was a default guess solution in the software when it was clear that $E_{min} > \phi_{sc}$ (i.e., for EDFs of Types C1 and C2). For reference, previous work has shown that typical ϕ_{sc} magnitudes for Wind in the solar wind are below ∼10 eV (e.g., Salem et al. 2001; Wilson et al. 2019a), consistent with the ϕ_{sc} estimates for Methods 2–4 shown in Figure 5.

The ϕ_{sc} estimates in Figure 5 also show an interesting solar cycle variation, consistent with other studies (e.g., C. S. Salem et al. 2023, in preparation). We focus on the peaks in the yellow-to-red color range as they have statistically significant counts. The histograms for Method 2 (second panel from top) show a bifurcated structure[12] in ϕ_{sc} that varies in time (Method 4 shows this, as well, but to a weaker extent). The first bifurcated peak occurs before 2006, which corresponds to the tail end of solar cycle 23 (see, e.g., trend in Diode 1 panel). The second bifurcated peak starts just before 2012 and extends to nearly 2016, which correponds to the peak in sunspot numbers (SSNs) for solar cycle 24 (also illustrated in trend in Diode 1 panel). Note that solar cycle 24 had a double-peaked structure

[10] We also list the one-variable statistics for the methods separated by EDF type in Appendix B.

[11] This was a default minimum we chose based upon the physically justified (and empirically motivated) assumption that the spacecraft will not charge negative in the solar wind in sunlight.

[12] That is, there are two peaks in the same time bin.

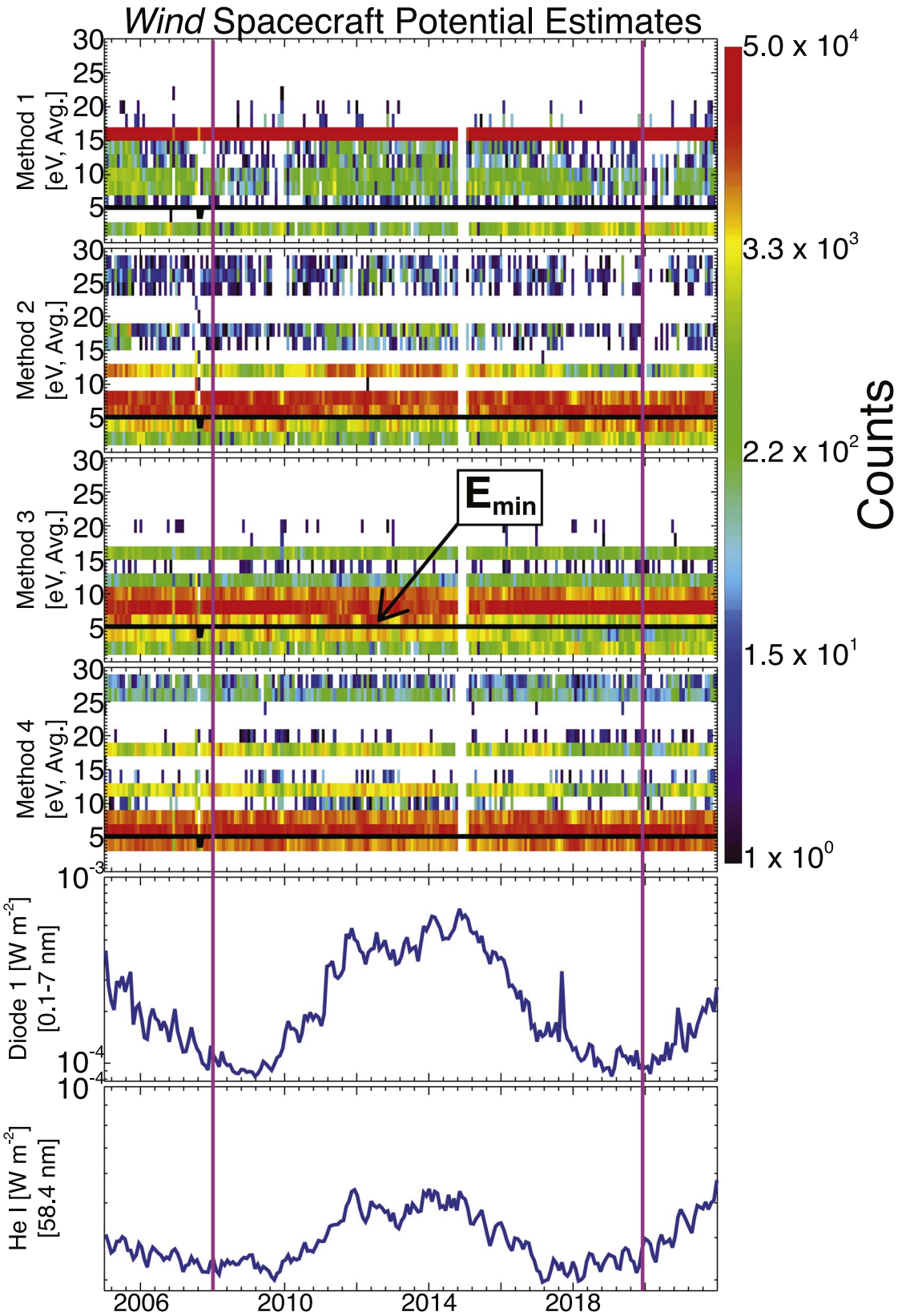


Figure 5. Two-dimensional histograms of the ϕ_{sc} estimates for Methods 1–4 (shown in order). The thick black line in each panel shows the E_{min} value vs. time. The horizontal (time) axis is parsed into 4 week bins while the vertical axis is parsed into 16 uniformly sized bins between 0 and 30 eV (i.e., roughly 2 eV each). The color scale shows total counts in each two-dimensional histogram bin. The bottom two panels show solar irradiances (in W m^{-2}) measured with two different detectors from the TIMED SEE experiment. These are shown as proxies for solar cycle variation and ionizing photon intensities vs. time. The two vertical magenta lines indicate the rough boundaries between solar cycles.

in SSNs, with the first peak just before 2012 and the second in early 2014. The last 3 yr of the data shown in Figure 5 are the start of solar cycle 25 corresponding to solar minimum, thus only a weak bifurcated peak is starting to show. Note that there is some hint of a third peak for Method 2 and Method 4 in Figure 5.

There are two environments known to enhance ϕ_{sc} in the solar wind: low-n_e regions and the sheath regions downstream of collisionless shock waves (e.g., Wilson et al. 2019a). The low-n_e regions have lower ambient electron currents, which increases the relative importance of the escaping photoelectron current, thus increasing ϕ_{sc} to more positive values. The sheath regions downstream of shock waves have much stronger ion currents, which increase ϕ_{sc} to more positive values. Interplanetary (IP) shock waves driven by coronal mass ejections (CMEs; e.g., Jian et al. 2006a; Richardson et al. 2018) and/or stream interaction regions (SIRs; e.g., Jian et al. 2006b; Richardson et al. 2018) are more common during solar maximum than solar minimum, thus show a clear solar cycle variation. Hence, the bifurcated peak likely occurs because of IP shock waves. As stated above, we are not implying that the solar irradiance changes versus time directly result in larger ϕ_{sc}. Rather, the solar irradiance measures are proxies for solar cycle variations, which directly influence the rate of CME and SIR occurrence.

The magnitude of ϕ_{sc} is observed to increase downstream of IP shocks (e.g., Wilson et al. 2019a), which is likely due to increases in the ion currents relative to the electron thermal and photoelectron currents.[13] This drives the spacecraft more electrically positive as it reaches a new current balanced equilibrium. It may also be related to enhanced secondary-electron generation internal to the instrument, as seen on other spacecraft in shock sheaths (e.g., Gershman et al. 2017), but this is beyond the scope of the present study.

The main takeaway from Table 1 and Figure 5 is that for the majority of the mission, the condition $5\,\mathrm{eV} \lesssim \phi_{sc} \lesssim 13\,\mathrm{eV}$ is satisfied, with peak occurrence rates in the ~6–9 eV range. In fact, most of the intervals where $\phi_{sc} \gtrsim 9\,\mathrm{eV}$ correspond to the sheath regions of IP shocks (see, e.g., discussion in Wilson et al. 2019a) because the ion thermal currents are much larger than in the ambient solar wind.

Figure 6 shows the PSD of all ϕ_{sc} estimates for all four EDF types (using Method 4) versus frequency. We also superposed the corresponding frequency of the synodic Carrington rotation period (~27.2753 days) and its first three harmonics. One can immediately see that ϕ_{sc} peaks at this frequency and its harmonics. The most likely explanation is due to the variations in $j_{th,s}$ and $j_{o,s}$ caused by SIRs (e.g., Jian et al. 2006b; Richardson et al. 2018), which typically occur at intervals defined roughly by the Carrington rotation of the Sun. We examined both the synodic (~27.2753 days) and sidereal (~25.38 days) periods, but the one of relevance is the synodic. An interesting observation is that these peaks are much less well defined when we construct the PSD using only Types A and B and are completely missing if we look at Type C1 or C2 or both C1 and C2. It is not immediately clear why the peaks change in amplitude or disappear altogether when isolating the different EDF types. However, this is beyond the scope of the current study.

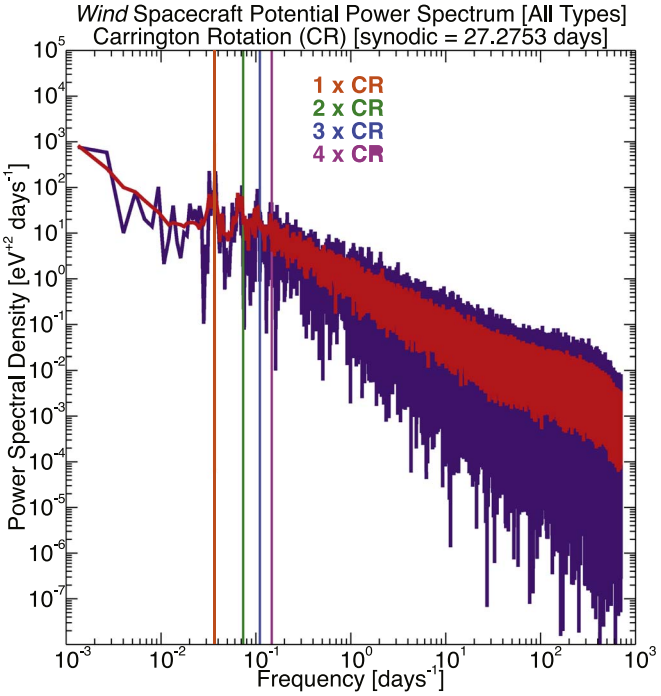


Figure 6. The power spectral density (PSD) (eV^{+2} days^{-1}) of the fast Fourier transform of all ϕ_{sc} estimates for all four EDF types, using Method 4 (note this is the median of the three PADs), versus frequency (days^{-1}) shown in purple. The red line is the smoothed PSD, using a running boxcar average with an eight-point bin width. Overplotted are four vertical lines corresponding to the frequency of the synodic Carrington rotation period (~27.2753 days) and its first three harmonics.

4. Discussion and Conclusions

We present measurements of the spacecraft floating potential for the Wind spacecraft near 1 au in the solar wind between 2005 January 1 and 2022 January 1 (i.e., over 17 yr). The analysis was performed as the first step in an effort to properly calibrate the Wind 3DP thermal electron detector, EESA Low. We describe the resulting publicly available data set and some preliminary results of the long-term statistical trends.

The long-term, statistical estimate for ϕ_{sc} satisfies $5\,\mathrm{eV} \lesssim \phi_{sc} \lesssim 13\,\mathrm{eV}$, with peaks in the ~6–9 eV range, consistent with previous measurements in the solar wind (e.g., Salem et al. 2001). Note that part of the reason for the small magnitudes of ϕ_{sc} is that Wind was designed and built with strict requirements for electromagnetic and electrostatic cleanliness (see, e.g., Wilson et al. 2021, and references therein). This is an important consideration in mission development and instrument calibration, as less stringent requirements lead to larger ϕ_{sc}, which will result in larger deviations between the observed energy–angle of an incident particle versus its true energy–angle (e.g., Barrie et al. 2019).

When we examined the statistical trends of ϕ_{sc} versus time, we found a bifurcated peak that correlated with solar maximum.[14] This is most likely due to enhanced ion currents downstream of IP shocks and/or regions of high ion temperature and low total electron density. We also found peaks in the power spectral density at the frequency corresponding to the synodic Carrington rotation period (~27.2753 days) and its first three

[13] That is, the ion temperature typically increases much more than the electron temperature in shock sheath regions, which increases the ion thermal currents more than the electron.

[14] A one-dimensional cut through the second peak for Method 2 in Figure 5 shows the count rates of this higher peak vary in phase with the solar irradiance measures shown at the bottom of Figure 5, i.e., they are highly correlated.

harmonics. The obvious candidates that depend upon Carrington rotation and solar cycle are SIRs and CMEs.

A critical takeaway from this study is that future thermal electron instrument design should require that $E_{\rm min} < \phi_{\rm sc}$ (for positive $\phi_{\rm sc}$) for the largest fraction of the measurements possible in any given region of space. This is critical for two reasons. The first is that when $E_{\rm min} < \phi_{\rm sc}$, the instrument is measuring all ambient electrons within its field of view as they are accelerated to energies of at least $e\phi_{\rm sc}$ before entering the detector (for positive $\phi_{\rm sc}$). If $E_{\rm min} > \phi_{\rm sc}$, the instrument does not measure all ambient electrons and, in fact, misses most of the velocity distribution. This can result in highly inaccurate velocity moments and affect the interpretation of any analysis performed on the data (e.g., Song et al. 1997; Wilson et al. 2022). There are ways to estimate $\phi_{\rm sc}$ when $E_{\rm min} > \phi_{\rm sc}$, as previously discussed (see, e.g., Salem et al. 2001, 2023). However, it requires multiple assumptions and very well calibrated instrumentation.

The second reason one should require that $E_{\rm min} < \phi_{\rm sc}$ is that it gives at least one direct, independent measure of $\phi_{\rm sc}$. That is, the observed "kink-like" change in the EDF as illustrated in the example in Figure 2 does not depend upon corrections to the instrument geometric factor or anode efficiencies. It only requires knowledge of the energy bin values, which is one of the most well-known parameters in a particle detector. The ability to directly determine $\phi_{\rm sc}$ from the particle data enables missions that do not have a direct measure of $\phi_{\rm sc}$ from an electric field instrument to properly calculate velocity moments and/or perform analysis on the electron velocity distributions. It can also provide a sanity check to help calibrate electric field measurements that directly measure $\phi_{\rm sc}$.

As previous efforts have shown (e.g., Song et al. 1997; Génot & Schwartz 2004; Lavraud & Larson 2016), properly correcting the electron measurements for $\phi_{\rm sc}$ is critical for calculating any velocity moments and/or instability analysis. In fact, poor estimates of $\phi_{\rm sc}$ or low-resolution instrumentation or instruments with $E_{\rm min} > \phi_{\rm sc}$ can result in velocity moment errors from ~10% to 30% to over 100% (e.g., Song et al. 1997; Wilson et al. 2022). Therefore, it is essential that electron thermal particle detectors be designed such that $E_{\rm min} < \phi_{\rm sc}$.

Acknowledgments

The analysis software (Wilson 2021) used herein can be found at https://github.com/lynnbwilsoniii/wind_3dp_pros. The Wind 3DP level zero data files are publicly available at http://sprg.ssl.berkeley.edu/wind3dp/data/wi/3dp/lz/. Some of the results presented in this document rely on data measured from the Thermosphere Ionosphere Mesosphere Energetics and Dynamics (TIMED) Solar EUV Experiment (SEE). These data are available from the TIMED SEE website at https://lasp.colorado.edu/see/data/. These data were accessed via the LASP Interactive Solar Irradiance Datacenter (LISIRD) at https://lasp.colorado.edu/lisird/. The resulting data set of Wind spacecraft floating potential measurements are found at doi:10.5281/zenodo.8364797. We thank W. Dean Pesnell for help with solar observations and data sources.

Appendix A
Definitions

In this appendix, the symbols and notation used throughout will be defined. All direction-dependent parameters we use have the subscript j to represent the direction, where $j =$ tot for the entire distribution, $j = \parallel$ for the the parallel direction, and $j = \perp$ for the perpendicular direction, where parallel/perpendicular is with respect to the quasi-static magnetic field vector, $\boldsymbol{B}_o$ (in nanoteslas). Below are the symbol/parameters definitions:

1. *One-variable statistics*
   (a) $X_{\rm min} \equiv$ minimum.
   (b) $X_{\rm max} \equiv$ maximum.
   (c) $\bar{X} \equiv$ mean.
   (d) $\tilde{X} \equiv$ median.
   (e) $X_{25\%} \equiv$ lower quartile.
   (f) $X_{75\%} \equiv$ upper quartile.
   (g) $X_{y\%} \equiv y$th percentile.
   (h) $\sigma \equiv$ standard deviation.
   (i) $\sigma^2 \equiv$ variance.
2. *Fundamental parameters*
   (a) $\varepsilon_o \equiv$ permittivity of free space.
   (b) $\mu_o \equiv$ permeability of free space.
   (c) $c \equiv$ speed of light in vacuum (in kilometers per second) $= (\varepsilon_o\ \mu_o)^{-1/2}$.
   (d) $k_{\rm B} \equiv$ the Boltzmann constant (in joules per kelvin).
   (e) $e \equiv$ the fundamental charge (C).
3. *Plasma parameters*
   (a) $n_s \equiv$ the number density (in cubic centimeters) of species s.
   (b) $m_s \equiv$ the mass (in kilograms) of species s.
   (c) $Z_s \equiv$ the charge state of species s.
   (d) $q_s \equiv$ the charge (C) of species $s = Z_s\ e$.
   (e) $T_{s,j} \equiv$ the scalar temperature (in eV) of the jth component of species s.
   (f) $V_{Ts,j} = \sqrt{\frac{2\ k_{\rm B}\ T_{s,j}}{m_s}} \equiv$ the most probable thermal speed (in kilometers per second) of a one-dimensional velocity distribution.
   (g) $\boldsymbol{V}_{\rm os} \equiv$ the drift velocity (in kilometers per second) of species s in the plasma relative to a specified rest frame.
   (h) $\phi_{\rm sc} \equiv$ the scalar, quasi-static spacecraft potential (in eV) (e.g., Scime et al. 1994; Pulupa et al. 2014).
   (i) $E_{\rm min} \equiv$ the minimum energy bin midpoint value (in eV) of a particle detector.
   (j) $E_{\rm max} \equiv$ the maximum energy allowed when finding $\phi_{\rm sc}$ from the particle data.
   (k) $j_{{\rm th,s}} = q_s\ n_s\ V_{\rm Ts,tot} \equiv$ the thermal current density (in μA m^{-2}) due to the ambient plasma species s.
   (l) $j_{o,s} = q_s\ n_s\ |V_{\rm os}| \equiv$ current density (in μA m^{-2}) due to ambient plasma species s drifting relative to the spacecraft.
   (m) $j_{\rm ph} \equiv$ the photoelectron current density (in μA m^{-2}).
   (n) $j_{\rm 2nd,s} \equiv$ the current density (in μA m^{-2}) due to secondary particles of species s emitted from the spacecraft due to impact ionization.
   (o) $f_s(E) \equiv$ energy distribution function (EDF) of particle species s.
   (p) $f_{\rm med}(E) \equiv$ the median of $f_s(E)$ at each energy over all solid angles.

Appendix B
Extra Statistics

In this appendix, we provide additional one-variable statistics of our estimates for $\phi_{\rm sc}$ separated by EDF types. Note that we only show Types A and B here, as Types C1 and

Table 2
Type A EDFs

ϕ_{sc} (eV)	X_{min}	$X_{5\%}$	$X_{25\%}$	$\bar{X}$	$\tilde{X}$	$X_{75\%}$	$X_{95\%}$	X_{max}
All 4,014,873 Type A EDFs, Lower Bound								
Method 1	1.00	1.00	5.18	4.96	5.18	5.18	5.18	17.3
Method 2	1.00	1.00	5.67	6.54	7.09	7.09	8.48	17.3
Method 3	1.00	1.00	5.18	5.14	5.18	5.93	5.93	12.7
Method 4	4.91	5.13	5.93	7.02	7.41	7.41	9.27	29.7
All 4,014,873 Type A EDFs, Upper Bound								
Method 1	4.91	5.13	29.7	27.7	29.7	29.7	29.7	29.7
Method 2	4.91	5.13	6.20	7.37	7.75	7.75	9.27	19.0
Method 3	4.91	5.13	12.7	13.2	12.7	12.7	18.1	29.7
Method 4	4.91	5.13	7.09	7.28	7.41	7.41	9.27	29.7

Note. Symbol definitions are the same as in Table 1.

Table 3
Type B EDFs

ϕ_{sc} (eV)	X_{min}	$X_{5\%}$	$X_{25\%}$	$\bar{X}$	$\tilde{X}$	$X_{75\%}$	$X_{95\%}$	X_{max}
All 4,213,734 Type B EDFs, Lower Bound								
Method 1	1.00	5.18	5.18	5.18	5.18	5.18	5.18	6.48
Method 2	1.00	8.48	8.87	9.96	9.27	11.6	12.7	27.1
Method 3	1.00	5.18	5.18	5.31	5.18	5.18	5.93	16.6
Method 4	5.13	5.93	6.48	9.26	9.27	9.70	18.1	29.7
All 4,213,734 Type B EDFs, Upper Bound								
Method 1	5.13	29.7	29.7	29.3	29.7	29.7	29.7	29.7
Method 2	5.13	9.27	9.70	10.9	10.1	12.7	13.9	29.7
Method 3	5.13	5.93	6.48	12.5	12.7	18.1	18.1	29.7
Method 4	5.13	5.93	6.48	10.7	9.70	12.7	18.1	29.7

Note. Symbol definitions are the same as in Table 1.

C2 have $E_{min} > \phi_{sc}$ and thus we cannot properly measure ϕ_{sc} from the thermal electron EDFs.

Table 2 shows one-variable statistics for only Type A EDFs, while Table 3 shows one-variable statistics for only Type B EDFs. Note that we have added the 25th and 75th percentiles to these tables for extra detail.

Appendix C
Public Data Set

In this section, we describe the variables that are included in the public data set (Wilson et al. 2023) and list where to find them.

Below, we describe the variables in the public data set and we use generic characters to define the number of elements in an array. We define N as the total number of EDFs (e.g., ~8,804,545 for entire data set, but will vary by year), P as the number of pitch-angle bins (i.e., 3), and R as the number of bounds or limits for any given estimtae (i.e., 2). The array dimensions will be shown in brackets, with each dimension separated by a comma. The public data set will include the following variables:

Unix: [N,R]-element (numeric) array of Unix[15] start and end times (in seconds).

YMDB: [N,R]-element (character string) array of UTC start and end times with format "YYYY-MM-DD/hh:mm:ss.xxx".

PosCurv: [N,P,R]-element (numeric) array of ϕ_{sc} (eV) estimates calculated from Method 1 (i.e., positive curvature region).

InflPnt: [N,P,R]-element (numeric) array of ϕ_{sc} (eV) estimates calculated from Method 2 (i.e., local minimum of $f_e(E)$).

MinMaxC: [N,P,R]-element (numeric) array of ϕ_{sc} (eV) estimates calculated from Method 3 (i.e., region of minimum and maximum curvature).

MinEflx: [N,P]-element (numeric) array of ϕ_{sc} (eV) estimates calculated from Method 4 (i.e., local minimum in $f_e(E)$).

MinEner: [N]-element (numeric) array of the instrument E_{min} values (eV).

MaxEner: [N]-element (numeric) array of the E_{max} values [eV] chosen a priori to bound the solutions for ϕ_{sc}.

EDFType: [N]-element (character string) array of EDF types (e.g., "A" for Type A).

QFlag: [N]-element (integer) array of quality flags based upon EDF types (e.g., 4 for Type A).

Note that the values for each of these have not been altered from those returned by the automated software performing these tests. For instance, we have not adjusted results from Method 3 for EDFs of Type C1 or C2. We left the original values in place and allow the user to alter the upper/lower bounds as they see fit for their own purposes. In general, for EDFs of Type C1 or C2 with shapes matching that shown in Figure 3, $\phi_{sc} < E_{min}$ for all four methods. This is why they are given a QF of zero. However, one should note that such EDFs and associated ϕ_{sc} are not useless or meaningless. These times are intervals where we can confidently define an absolute upper bound on ϕ_{sc}. They also correspond to times when ϕ_{sc} is very small, relative to the typical values shown in Figure 5 and Table 1.

The data set will consist of a list of yearly ASCII files from 2005 January 1 to 2022 January 1. More years can be added as time progresses to expand the data set. This data set is the first step toward generating a properly calibrated electron velocity moment data product for public consumption. The next step requires the knowledge of the total electron density from the upper hybrid line, a data set that is currently in production (e.g., see Martinović et al. 2020 for details). The combination of accurate estimates from these two quantities will allow us to update the anode calibrations for the Wind 3DP thermal electron detector, EESA Low.[16] Note that spacecraft charging can also affect the trajectories of incident low-energy particles (see, e.g., Barrie et al. 2019 for details). However, this would require an accurate model of the Wind spacecraft surface materials and the evolution of their work functions over time, which is beyond the scope of this effort.

Finally, we should note that the data set Salem & Pulupa (2023) provided by and discussed in Salem et al. (2023) does not overlap with this new data set and it spans the interval when $E_{min} > \phi_{sc}$, early in the Wind mission. Thus, Salem et al. (2023) relied on different techniques to estimate ϕ_{sc} than the methods described herein. The measurements in Salem et al. (2023) are also subject to smaller variations in the anode calibrations than the measurements made later in the mission (i.e., the data herein).

[15] Note that the times are not really Unix times, as they include leap seconds from UTC time conversions. The UMN software discussed in the Acknowledgments section handles this accordingly.

[16] In the unit-conversion process, this calibration enters through a modification to the optical geometric factor for each energy–angle bin. It is important to note that these calibrations do not affect the detector energy bin values, i.e., they will not affect ϕ_{sc} for the methods used herein.

This was shown in a recent study (see, e.g., the Appendices of Wilson et al. 2019a) in some example anode correction calculations for the time period examined by Salem et al. (2023). Thus, they were able to estimate ϕ_{sc} numerically from the difference between the total electron density calculated from the upper hybrid line and that calculated by numerically integrating the velocity distribution. They iteratively modify ϕ_{sc} until the numerically integrated electron density matches that from the upper hybrid line. This is a well-known and valid approach when $E_{min} > \phi_{sc}$, assuming the instrument anodes and energy–angle geometric factors are properly calibrated.

ORCID iDs

Lynn B. Wilson III https://orcid.org/0000-0002-4313-1970
Chadi S. Salem https://orcid.org/0000-0002-6536-1531
John W. Bonnell https://orcid.org/0000-0002-0675-7907

References

Bame, S. J., Hundhausen, A. J., Asbridge, J. R., & Strong, I. B. 1968, PhRvL, 20, 393
Barrie, A. C., Cipriani, F., Escoubet, C. P., et al. 2019, PhPl, 26, 103504
Besse, A. L., & Rubin, A. G. 1980, JGR, 85, 2324
Bochsler, P., Geis, J., & Joos, R. 1985, JGR, 90, 10779
Bougeret, J.-L., Kaiser, M. L., Kellogg, P. J., et al. 1995, SSRv, 71, 231
Ergun, R. E., Tucker, S., Westfall, J., et al. 2016, SSRv, 199, 167
Garrett, H. B. 1981, RvGSP, 19, 577
Geach, J., Schwartz, S. J., Génot, V., et al. 2005, AnGeo, 23, 931
Génot, V., & Schwartz, S. 2004, AnGeo, 22, 2073
Gershman, D. J., Avanov, L. A., Boardsen, S. A., et al. 2017, JGRA, 122, 11548
Gloeckler, G., Cain, J., Ipavich, F. M., et al. 1998, SSRv, 86, 497
Grard, R., Knott, K., & Pedersen, A. 1983, SSRv, 34, 289
Grard, R. J. L. 1973, JGR, 78, 2885
Halekas, J. S., Whittlesey, P., Larson, D. E., et al. 2020, ApJS, 246, 22
Jian, L., Russell, C. T., Luhmann, J. G., & Skoug, R. M. 2006a, SoPh, 239, 393
Jian, L., Russell, C. T., Luhmann, J. G., & Skoug, R. M. 2006b, SoPh, 239, 337
Lai, S. T., Martinez-Sanchez, M., Cahoy, K., et al. 2017, ITPS, 45, 2875
Lavraud, B., & Larson, D. E. 2016, JGRA, 121, 8462
Lepri, S. T., Landi, E., & Zurbuchen, T. H. 2013, ApJ, 768, 94
Lin, R. P., Anderson, K. A., Ashford, S., et al. 1995, SSRv, 71, 125
Lindqvist, P.-A., Olsson, G., Torbert, R. B., et al. 2016, SSRv, 199, 137
Martinović, M. M., Klein, K. G., Gramze, S. R., et al. 2020, JGRA, 125, e28113
Maruca, B. A., Bale, S. D., Sorriso-Valvo, L., Kasper, J. C., & Stevens, M. L. 2013, PhRvL, 111, 241101
Meyer-Vernet, N., & Perche, C. 1989, JGR, 94, 2405
Pedersen, A. 1995, AnGeo, 13, 118
Phillips, J. L., Bame, S. J., Gosling, J. T., et al. 1993, AdSpR, 13, 47
Pulupa, M. P., Bale, S. D., Salem, C., & Horaites, K. 2014, JGRA, 119, 647
Richardson, I. G., Mays, M. L., & Thompson, B. J. 2018, SpWea, 16, 1862
Salem, C., Bosqued, J.-M., Larson, D. E., et al. 2001, JGR, 106, 21701
Salem, C., Hubert, D., Lacombe, C., et al. 2003, ApJ, 585, 1147
Salem, C. S., Pulupa, M., Bale, S. D., & Verscharen, D. 2023, A&A, 675, A162
Salem, C. S., & Pulupa, M. P. 2023, Wind 3DP Electron Core Halo Strahl Moments, 96s, year files, v2.5.0, NASA Space Physics Data Facility, doi:10.48322/rgf7-3h67
Scime, E. E., Phillips, J. L., & Bame, S. J. 1994, JGR, 99, 14769
Scudder, J. D., Cao, X., & Mozer, F. S. 2000, JGR, 105, 21281
Song, P., Zhang, X. X., & Paschmann, G. 1997, P&SS, 45, 255
Whipple, E. C. 1981, RPPh, 44, 1197
Wilson, L. B., III 2021, Space Plasma Missions IDL Software Library, v1.0.2, Zenodo, doi:10.5281/zenodo.6141586
Wilson, L. B., III, Brosius, A. L., Gopalswamy, N., et al. 2021, RvGeo, 59, e2020RG000714
Wilson, L. B., III, Chen, L.-J., Wang, S., et al. 2019a, ApJS, 243
Wilson, L. B., III, Chen, L.-J., Wang, S., et al. 2019b, ApJS , 245
Wilson, L. B., III, Goodrich, K. A., Turner, D. L., et al. 2022, FrASS, 9, 1063841
Wilson, L. B., III, Salem, C. S., & Bonnell, J. W. 2023, Wind spacecraft floating potential measurements, v1.0, Zenodo, doi:10.5281/zenodo.8364797
Wilson, L. B., III, Stevens, M. L., Kasper, J. C., et al. 2018, ApJS, 236, 41
Woods, T. N., Eparvier, F. G., Bailey, S. M., et al. 2005, JGR, 110, A01312